Nano Energy 133 (2025) 110483

Contents lists available at ScienceDirect

Nano Energy

journal homepage: www.elsevier.com/locate/nanoen

Photovoltaic windows based on ultrathin transition-metal dichalcogenides: Natural indoor illumination spectra and energy-saving potential

Carlos Bueno-Blanco [a], Simon A. Svatek [a,*], Francisco M. Gomez-Campos [b], Antonio Marti [a], Elisa Antolin [a,*]

[a] Instituto de Energía Solar, Universidad Politécnica de Madrid, Avenida Complutense 30, Madrid 28040, Spain
[b] Departamento de Electrónica y Tecnología de los Computadores, Facultad de Ciencias, Universidad de Granada, Av. Fuentenueva s/n, Granada 18071, Spain

ARTICLE INFO

Keywords:
Semitransparent solar cell
Building-integrated photovoltaics
Ultrathin solar cell
2D material
Transition metal dichalcogenide

ABSTRACT

Semitransparent photovoltaic windows are attractive for building-integrated applications because they can regulate natural indoor illumination while generating power. In this work, we assess the potential of transition metal dichalcogenide (TMDC) semitransparent solar cells as emerging technology for this application. We model a semitransparent ultrathin photovoltaic device containing a MoS_2 or WSe_2 absorber and find that it can be optimized to produce a balanced absorption of the sunlight spectrum because of the unique optical properties of these materials, eliminating the common problem of the undesired coloring of the transmitted light. The device also exhibits high angular absorptance. We estimate a potential saving between 16 % (winter) and 23 % (summer) in the electricity consumption of a high-rise office building located in Madrid, Spain, by implementing TMDCs semitransparent windows with an average photopic transmission (APT) of 24 %. Notably, this is compatible with a high quality in the transmitted light: the color rendering index (CRI) of the PV windows exceeds 90 for an APT between 23 % and 65 %. These results, along with the fact that TMDCs can be deposited using low-cost, scalable methods, indicate that TMDCs hold great potential for developing color-neutral, power-generating building glazing.

1. Introduction

Large non-domestic buildings are responsible for an important share of the electricity demand in most countries. In Spain, for example, the consumption of buildings dedicated to tertiary sector activities was 74.6 TWh in 2019, around 28 % of the total consumed electricity [1]. For these buildings to improve their energy balance it is crucial to exploit the sunlight reaching their large façade areas [2–4]. This can be done by implementing semitransparent photovoltaic devices on glazed curtain walls. Moreover, semitransparent photovoltaics can be used to control indoor temperature and illumination. Unfiltered sunlight provides illumination levels reaching 100,000 lux whereas the official recommendations for offices are between 200 and 500 lux [5]. To curtail excessive light and heat, filtering sunlight with power-generating windows would be more beneficial than the currently established solution of using highly reflective windows. Photovoltaic windows would not only produce electrical power, but they would also prevent glare that affects pedestrians and drivers [6] and they would help maintain the thermal balance of urban areas, as highly reflective windows have been shown to overheat the surrounding asphalt [7].

The first challenge in the design of semitransparent solar cells is reaching a positive trade-off between generated power and transmitted light. Using the conventional technology based on crystalline silicon (c-Si), semitransparency is only achieved by intercalating solar cells with transparent materials [8]. The resulting patchy lighting is usually not appropriate for working environments. A possible solution to this problem has been proposed through the drilling of micro-holes in bare c-Si wafers, showing a lab-scale power conversion efficiency (PCE) of 12.2 % and associated transmittance of 20 % (or PCE 7.4 % and transmittances 50 %) [9]. Amorphous Si solar cells can be semitransparent reducing the thickness of the active layer, leading to flexible applications that achieve a PCE of 5 % and an average transmittance of 34 % [10]. In addition to silicon, other technologies such as thin film, organic, dye-synthesized, and hybrid perovskite have emerged as candidates for semitransparent applications [11,12]. Organic photovoltaics are particularly interesting because of their potential to absorb infrared

* Corresponding authors.
E-mail addresses: simon.svatek@upm.es (S.A. Svatek), elisa.antolin@upm.es (E. Antolin).

https://doi.org/10.1016/j.nanoen.2024.110483
Received 4 August 2024; Received in revised form 28 October 2024; Accepted 16 November 2024
Available online 19 November 2024

frequencies that are not perceptible to the human eye. An organic-based device has been reported that reaches a PCE of 10.8 % and an average transmission of 45.7 % [13]. For all these emerging technologies, the optimization of the chromatic characteristics of the transmitted light is an important problem [11]. In some cases, a layer is included that absorbs a range of the solar spectrum, allowing for color neutrality at the cost of introducing a mechanism of power loss [12].

Layered and 2D materials, such as transition metal dichalcogenides (TMDCs), are a promising and yet unexplored solution for semi-transparent power-generating windows. These materials show outstanding optical properties even in the form of ultrathin laminae [14, 15]. They are chemically stable [16] and composed of elements relatively abundant in the Earth's crust compared to traditional materials used in thin-film devices [17,18]. Furthermore, due to the self--passivated nature of TMDC crystals, simply bringing TMDC laminae into physical contact at room temperature enables the fabrication of extremely thin devices - van der Waals structures - which can be flexible and durable [19]. TMDC solar cells, therefore, have the potential to achieve very high specific power and the low material requirements can translate into low fabrication costs [18].

Although the technology for opaque TMDC solar cells is still under development, photovoltaic devices have been demonstrated over the past decade [20–23], with important milestones achieved. This includes the measurement of a 1 V open-circuit voltage in a MoS_2 device with a bandgap energy of 1.3 eV [24], and a conversion efficiency of 5.1 % with a specific power of 4.4 W g^{-1} in a WSe_2 device [25]. Additional significant experimental results can be found here [26,27]. Regarding the potential for efficiency improvements in this emerging technology, a detailed-balance analysis incorporating non-idealities has shown that single-junction solar cells made of films as thin as 50 nm could in practice achieve up to 25 % power conversion efficiency with the currently available material quality [28]. Another study, examining a WSe_2 solar cell fabricated by tungsten selenization, a low-cost method, suggests that 22 % efficiency may be achievable [29]. If the solar cell contains a stack of isolated TMDC monolayers instead of an ultrathin bulk TMDC absorber - the so-called excitonic TMDC solar cell- the practical efficiency limit is lower (13 %) [18].

In this work, we propose a design of a semitransparent window based on an ultrathin bulk layer of a TMDC (see Fig. 1.a). We have applied the model to MoS_2 and WSe_2 devices because these materials are the most studied among TMDCs. We optimize the structure to provide a significant PCE while maintaining high-quality indoor illumination, which requires that the windows are color neutral. Color neutrality means here that the transmitted spectrum is sufficiently close to a black-body spectrum of any temperature, which means that the coloring will be natural to the human eye. This approach is widely used for LEDs, but it is not common in the analysis of semitransparent windows. Most experimental results from perovskite, organic and thin-film transparent solar cells show distortions of the spectrum ranging into unnatural yellow, brown or red shades, and color neutrality is often understood as the need to achieve an unaltered spectrum when the light goes through the device [9,11,12]. We will show that the unique absorption coefficients of

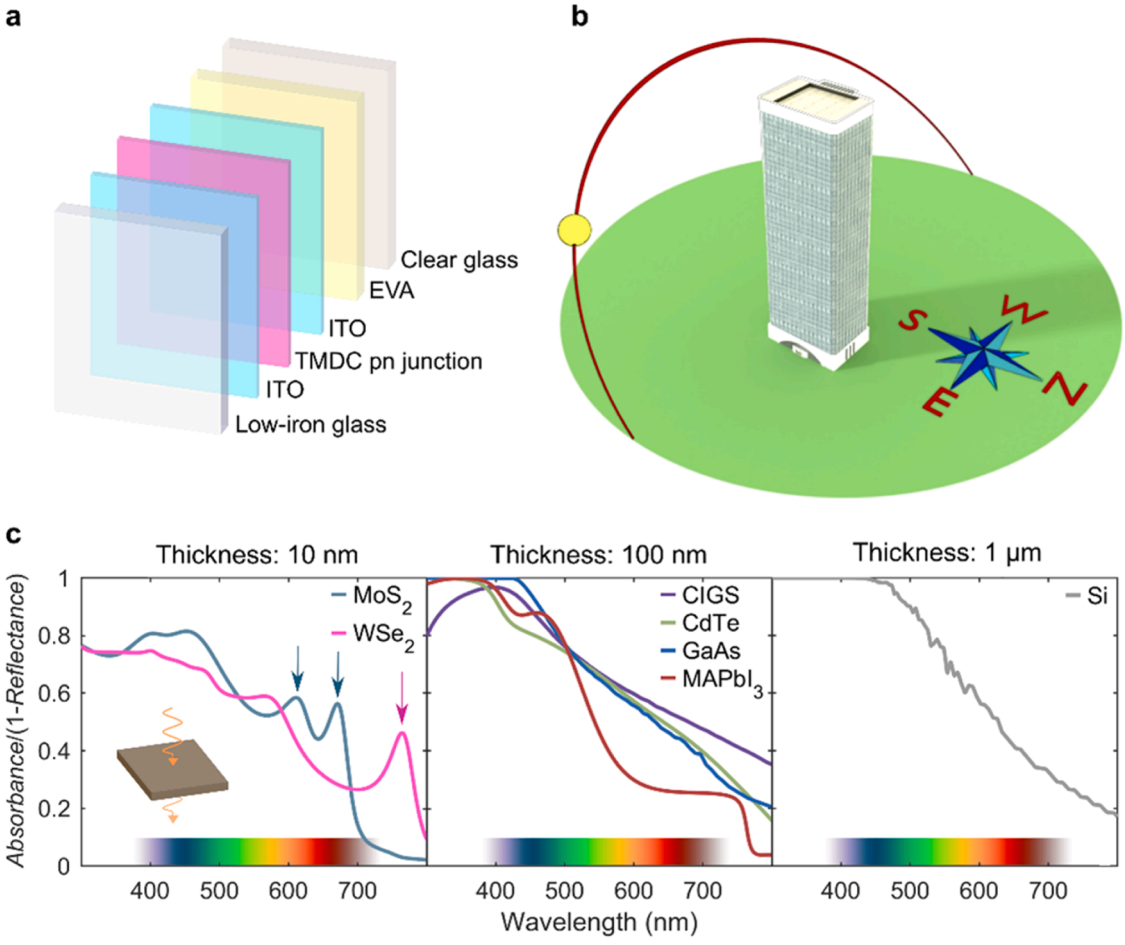

Fig. 1. Description of the proposed TMDC-based semitransparent power-generating windows. (a) Layer structure. (b) Orientation of the Picasso Tower in Madrid that will be used as case study for PV-window integration. (c) Fraction of the non-reflected light that gets absorbed in a single slab of different semiconductor materials: left, TMDCs (arrows mark excitonic peaks); middle, direct-gap semiconductors commonly used in photovoltaics; right, crystalline silicon. References for the refractive indexes to in the calculations: MoS_2 [35], WSe_2 [36], CIGS [37], CdTe[38], $MAPbI_3$ [39], GaAs [40] and silicon [40].

TMDCs allow them to modulate the solar spectrum, transforming it into a natural black-body spectrum of lower temperature instead of distorting it.

We analyze the angular acceptance and estimate the electrical power generation and light transmission for different façade orientations throughout the year. We model a range of TMDC thicknesses, including clear windows, with an average photopic transmission (APT) of around 60 %, and sun-control windows, with APT below 60 % down to 15 %, which are to be used in latitudes and orientations where the direct sunlight can hinder indoor activities. We simulate the interior illumination conditions of an office using Blender 3D [30] to show how TMDC-based semitransparent windows change the chromaticity of the incoming light. Finally, we analyze the Picasso Tower in Madrid (see Fig. 1.b) as an example of a large office building and estimate the possible electricity production if a TMDC power-generating glazing would cover the façades.

2. Design of TMDC-based semitransparent photovoltaic window

Fig. 1.a shows the proposed structure of a TMDC-based module wherein the solar cell is deposited between two indium-tin-oxide (ITO) layers which work as transparent electrical contacts. For the sake of cost-efficiency, this structure is expected to be built using solution-processed TMDC deposition on the front ITO/glass substrate with precise thickness control and homogeneity following, for instance, the polymer-assisted deposition method described in [31]. This method produces homogeneous layers down to 2 nm thickness. The layers present a low roughness for thickness below 15 nm and a moderate roughness for thickness between 15 and 30 nm. An alternative method for low-cost and scalable fabrication of WSe_2 is the selenization of tungsten, which has achieved high uniformity in ~20-nm-thick films, with smooth and uniform surfaces, and grain sizes comparable to the film thickness [29]. The TMDC slab represented in the figure contains a pn junction implemented through substitutional doping [24,32] (either a MoS_2 or a WSe_2 homojunction). We refer to it as the TMDC absorber. As in commercial solar modules, we use a high transmittance glass on the front cover (low-iron glass quality), whereas the back glass is a conventional architectural glass (clear glass quality) [33]. Both glasses have a thickness of 3.2 mm. As is also customary in PV, the module is encapsulated using a 0.45 mm thick insulant polymer (ethyl-vinyl acetate, EVA). No antireflecting layers have been inserted in the structure because, as we have already shown elsewhere for opaque devices [34], the front ITO layer has a close-to-optimum refractive index to produce an antireflective effect when located onto a TMDC layer.

Fig. 1.c illustrates the unique properties of TMDCs for semitransparent applications that have inspired this work. Firstly, their absorption coefficient is extraordinarily large. The light absorption in a self-standing slab of only 10 nm of MoS_2 or WSe_2 (left graph) is comparable to the absorption of 100 nm of conventional direct gap semiconductors (middle graph) or 1 μm of silicon (right graph). Note that in Fig. 1.c, to enable a fair comparison, we have represented the absorbed fraction from the light that is not reflected and actually enters the slab (when any of these materials is used in a solar cell it will be covered with an optimized antireflection layer). The second remarkable feature of the TMDC absorptance is that it presents strong excitonic peaks inherent to the partial carrier confinement produced by their layered structure [14,15]. These peaks enhance the absorption in the vicinity of the bandgap edge, producing a balanced absorption over the whole visible range. Contrarily, in layers of conventional materials, the blue part of the spectrum is more strongly absorbed than the red part, which leads to a reddish transmitted spectrum if the device is thick enough to produce a significant photocurrent [41]. The device optimization work presented here aims at exploiting this unique characteristic of TMDC semiconductors to design color-neutral power-generating windows.

Our optical model for ultrathin TMDC solar cells is based on the generalized scattering-matrix formalism (transfer-matrix method) described by Centurioni [42]. We apply it to the complete semitransparent module structure depicted in Fig. 1.a, supposing homogeneous multilayers. As mentioned above, current low-cost fabrication methods for large-area TMDC deposition already demonstrate high layer homogeneity within the thickness range relevant for semitransparent applications [29,31]. The transfer-matrix method allows us to combine coherent and incoherent layers, accounting for multiple reflections, as well as interference within the coherent layers. In our structure, the absorber and ITO layers are extremely thin, which leads to significant interference effects that impact light absorption and transmission. The validity of the transfer-matrix method for simulating strong interference effects has been widely assessed. In particular, it has been experimentally validated for ultrathin layers of highly absorbing media by Kats et al. [43]. The TMDC absorber is modeled as a single TMDC slab (we are neglecting possible effects of the p and n doping on the values of refractive index n and extinction coefficient k). The n and k anisotropy inherent to TMDCs [35,36] is taken into account. The TMDC absorber and ITO layers are considered coherent. This is justified in the Supporting Information (SI) section S5. The thicker EVA and glass layers are considered incoherent. More details on the optical model, the simulation of incident spectra, and the figures for the quantification of spectral quality are given in the Methods Section and the SI, sections S1 to S4. Our code of the optical model is published in the GitHub repository [44].

3. Absorptance and chromaticity of the transmitted spectrum

Fig. 2.a and b show the absorptance of the TMDC absorber (WSe_2 or MoS_2) when it is located inside the power-generating window structure shown in Fig. 1.a. Different absorber thicknesses are presented from 3 to 55 nm. For each absorber thickness, the bottom and top ITO layer thicknesses have been optimized using a two-criteria algorithm: (i) the TMDC absorption is maximized, and (ii) the transmitted spectrum must approach the chromatic characteristics of a natural light source following current solid-state illumination standards [5,45]. The second criterion will be further explained later in this section. Using this two-criteria algorithm implies that the optimum layer structure for a given absorber thickness is not necessarily the one that results in the highest possible absorption. Table 1 compiles the optimum top and bottom ITO thicknesses for each TMDC absorber thickness. The optimization has been performed at an incidence angle of 57°, which approximates the daily average incidence angle on a vertical window for our case of study (Madrid, coordinates 40° 24' N, 3° 42' W, vertical module, east and southeast orientation). The average incidence angle depends on both the latitude and the orientation of the active surface, although variations are not strong. For instance, the average angle for east orientation in London (51.5° N) is 58°, whereas in Sydney (33.8° S) it decreases to approximately 54°. Details about the calculation are available in the SI, Section 12.

Because interference effects are strong in these ultrathin devices, some TMDC thicknesses close to an interference maximum will produce especially high absorptances. This is the case of the 11- and 55-nm-thick absorbers in Fig. 2.a and b. The 55 nm absorber thickness corresponds to the first-order resonant maximum. The 11 nm-thick absorber thickness coincides with the zeroth-order resonance maximum, which can appear in highly absorbing media embedded between certain interfaces [43,46]. The zeroth-order resonance has been shown to produce very high, broadband absorption in opaque TMDC solar cells with a metal back reflector [34]. Further details on the interference maxima are given in the SI, section S4.

Fig. 2.c and d illustrate the chromatic quality of TMDC-based photovoltaic windows. They show the CIE 1931 color space, on which the white dots mark the chromatic coordinates associated to the spectral power distribution (SPD) of the light transmitted by the TMDC-based windows when they are illuminated by the AM1.5 G solar spectrum. Inside the CIE space, the black line represents the Planckian locus, which is the path that the color of a black body takes as its temperature changes

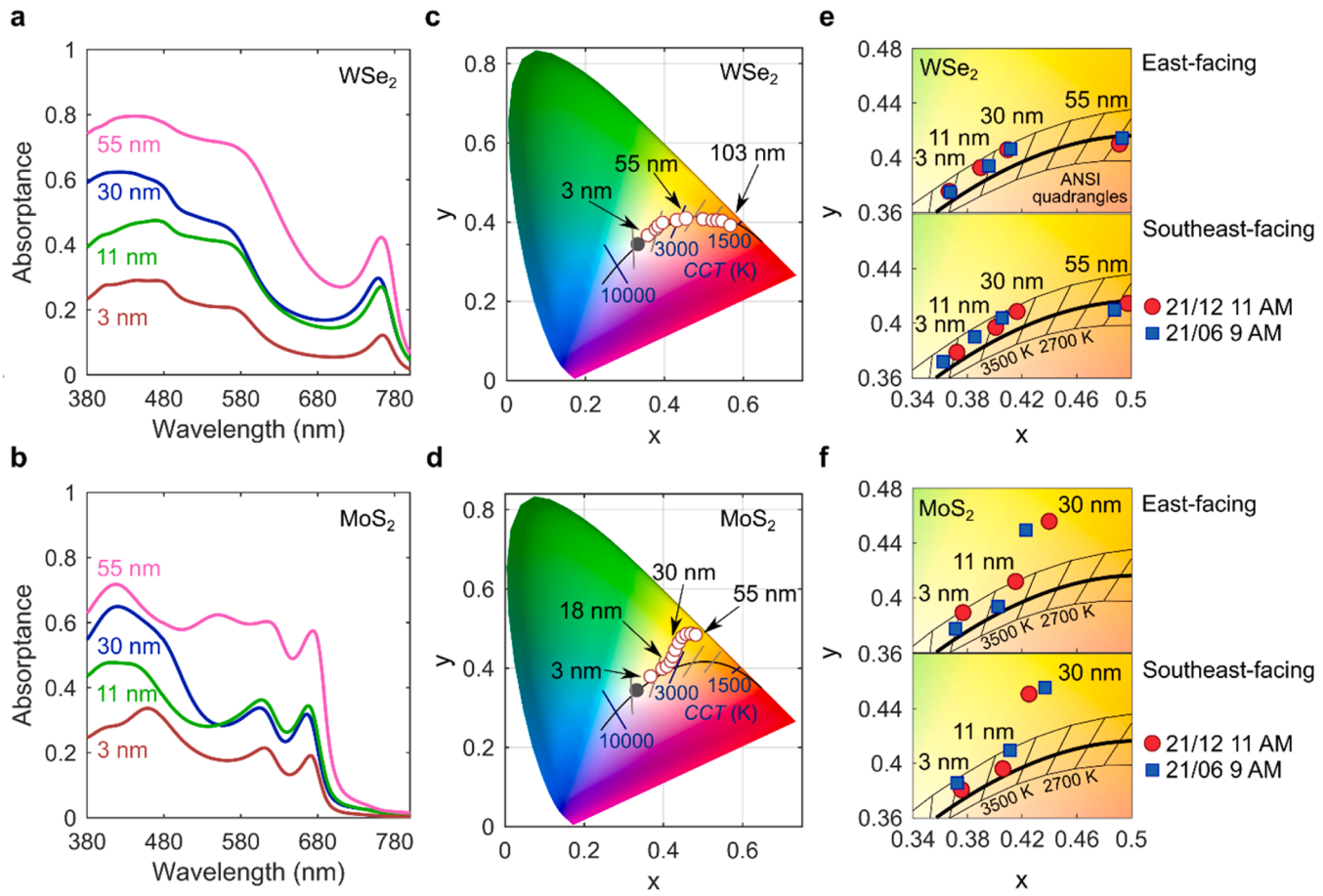

Fig. 2. Light absorption and chromaticity of photovoltaic windows. (a) (b) Incidence spectral absorptance of an optimized WSe_2 (MoS_2) absorber when it is located inside the module structure. The labels indicate the thickness of the TMDC absorber. (c) (d) CIE 1931 chromaticity space showing the spectra (white circles) transmitted by the PV-windows with different WSe_2 (MoS_2) thicknesses when they are illuminated with the AM1.5 G spectrum. Black labels indicate the thickness of the TMDC absorber. The black circle marks the coordinates of the AM1.5 G spectrum and the black line represents the Planckian locus. Blue labels indicate the CCT of different points along the Planckian locus. (e) (f) Zoomed-in view of the CIE 1931 chromaticity space showing the transmitted spectra under different illumination conditions: red circles mark the spectra transmitted by the WSe_2(MoS_2)-based windows if they are exposed to sunlight in Madrid at 11:00 AM on December 21st, and blue squares mark the transmitted spectra in Madrid at 9:00 AM on June 21st. East and southeast window orientations are shown for both cases. The thick black line is the Planckian locus, and the thinner lines define the ANSI C78.377 quadrangles.

Table 1
Optimized ITO layer thicknesses for MoS_2 and WSe_2 semitransparent power-generating windows with different absorber thicknesses.

MoS_2 semitransparent solar cell		
ITO top (nm)	MoS_2 (nm)	ITO bottom (nm)
161	3	154
152	11	150
150	30	145
WSe_2 semitransparent solar cell		
ITO top (nm)	WSe_2 (nm)	ITO bottom (nm)
123	3	127
91	11	110
62	30	91
54	55	207

from 10000 K to 1500 K. Therefore, this curve contains the illumination spectra that are natural to the human eye, from indirect sunlight (correlated color temperature, CCT, ~ 8000 K), over direct sunlight (CCT ~ 6000 K), to candlelight (CCT ~ 1500 K). Our optimization algorithm searches for the layer structure that provides the largest absorption while achieving a natural color of the transmitted light. We define this color condition as keeping a maximum distance of $5.4{\cdot}10^{-3}$ units in the CIE 1960 color space from the nearest point in the Planckian locus (this is the limit defined by the CIE standard [45]). We apply here the standards for LED illumination [47], which allow for a variable CCT and seek natural light spectra, in contrast to many publications on semitransparent solar cells [9,11,12] that define color neutrality as the capability of a window to reproduce the CIE coordinates of a reference illuminant (typically the AM1.5 G spectrum with CCT ~ 5500 K or the D65 white with CCT ~ 6500 K [45]).

In Fig. 2.c, d, the chromatic coordinates of the transmitted spectra from optimized window structures follow the Planckian locus, shifting to lower CCTs as the TMDC absorber thickness increases. In the case of WSe_2-based structures, the deviation from the Planckian locus is imperceptible up to an absorber thickness of 103 nm. It is remarkable that this is achieved without resorting to the addition of dyes or colored glass that would make the structure of the window more complex and introduce optical losses. MoS_2-based structures start to deviate from the Planckian locus at a much smaller thickness of 18 nm. This is a consequence of the larger bandgap energy of MoS_2, which leads to a stronger transmission of long-wavelength colors.

Fig. 2.e and f depict the central region of the CIE color space to show the chromaticity of the transmitted spectra for different realistic incident sunlight spectra. The incident spectra have been modelled for the latitude of Madrid, Spain, assuming an east or southeast window orientation, as they correspond to office working hours in which solar indoor

penetration is large. They include the direct and diffuse components of sunlight (see the Methods section and SI, section S3). Red circles correspond to the transmitted spectra on December 21st at 11:00 AM local time, and blue squares mark the transmitted spectra on June 21st at 9:00 AM local time. The plots include six quadrangles situated along the Planckian locus. The quadrangles define the space of acceptable chromatic coordinates for solid-state lightning products according to the ANSI C78.377 standard [47]. Spectra falling on each one of these quadrangles are considered to resemble a black body with the CCT written under that quadrangle (some accepted quadrangles of lower CCT are not shown in the figure).

Although the window layer structures have been optimized using only the AM1.5 G spectrum, Fig. 2.e and f show that the transmitted spectra calculated for different sunlight conditions also fulfill the chromaticity standards. The only exception on these graphs is the 30-nm thick MoS_2 absorber, which produces a non-natural yellowish spectrum because its thickness is beyond the 18 nm limit discussed above. Although non-color-neutral windows such as the 30 nm-thick MoS_2 window are not appropriate for illumination of working or living spaces, they could still be used with an aesthetic purpose in architectural designs that intend to change color perception [48,49].

The chromatic characteristics of TMDC structures for semitransparent applications presented here outperform those of traditional inorganic thin-film materials, particularly for highly absorbing devices [11]. They are comparable to those reported for organic devices of moderate absorption [13], although in that case it is unclear yet if color neutrality can be kept when the absorptance is very high. In this sense the TMDC structures also outperform other technologies, such as perovskite solar cells, which currently require the addition of colored absorbing layers to achieve color neutrality [12].

It is interesting to study the chromaticity of the transmitted spectrum throughout one day. Fig. 3 depicts the evolution of the chromaticity of the incident and transmitted light in Madrid on June 21st for an east-facing semitransparent window with a 30 nm-thick WSe_2 absorber. Both the incident and the transmitted light move along the Planckian locus throughout the day. Note that an east-oriented window will receive mostly direct sunlight at 9 AM and 12 PM (CCT ~ 5500 K), whereas at 3 PM and 6 PM only indirect sunlight will reach the window (CCT > 7000 K, in correspondence with the blue tone of the sky). All transmitted spectra fulfill the ANSI C78.377 standard. Their chromaticity is shifted to CCT values lower than those of the incident light, which makes the light produced by the windows more adequate for a working environment than direct sunlight (the recommended CCT for LED indoor illumination is between 5000 and 3300 K [47]). The fact that the photovoltaic window produces a natural light spectrum does not mean that it has no visual effect: an observer positioned behind it will see a sky color tending to white rather than blue.

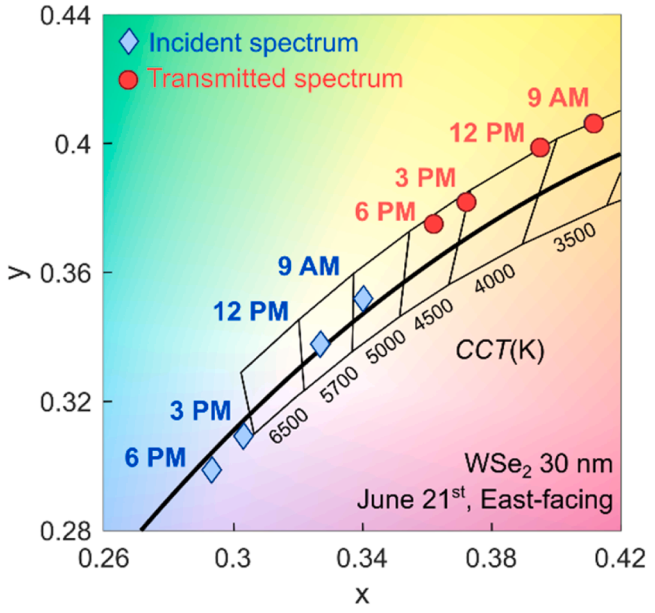

Fig. 3. Zoomed-in view of the CIE 1931 chromaticity space showing the daily evolution of the incident sunlight spectrum (blue diamonds) and the spectrum transmitted by the PV window (red circles). The window was modeled containing a 30 nm-thick WSe_2 absorber and it is oriented east-facing on June 21st in Madrid. APT of the window at 9 AM is 24 %.

We will now introduce two additional figures to characterize the light transmitted by the power-generating windows: color rendering index (CRI) and average photopic transmission (APT). The APT determines the percentage of visible light transmitted through the window and it is used to quantify the brightness perceived by the human eye. In the case of architectural glass APT values above 60 % look clear. Values below that benchmark are considered dark and employed in locations where direct sunlight must be curtailed [50]. The CRI quantifies to which extent the color perceived when looking at an object illuminated with a given spectrum resembles the natural color of that object. A CRI value of 80 is the general baseline for most indoor and commercial lighting applications. Spaces where color appearance is particularly important, such as a graphic design office, would probably require a CRI of 90 and above.

Table 2 shows the values obtained for the transmitted spectra included in Fig. 2.e(f). Logically, windows implementing thinner TMDC absorbers exhibit higher APT and CRI values. Both MoS_2 and WeS_2 absorbers with a thickness of 3 nm provide CRI > 90 and APT > 60 % making the photovoltaic window appropriate to produce clear illumination in demanding environments such as hospitals or printing facilities. Thicker absorbers still provide an acceptable CRI, but ATP values are low. Such devices are useful in situations where direct sunlight is excessive. Office buildings in sunny locations face the paradox of receiving such intense solar flux that they need to block it and instead use artificial indoor lighting. In this context, semitransparent windows play a dual role in the energy balance: not only do they generate electrical power from excess solar flux, but they also filter the transmitted light, adapting it to indoor lighting needs and providing additional energy savings by reducing the need for artificial lighting. In this respect it is remarkable that CRI > 80 can be achieved by WSe_2-based windows for APT values as low as 13 %. The CRI of the 30-nm-thick MoS_2 window cannot be calculated because the chromatic coordinates of the transmitted SPD are too far from the Planckian locus [45].

To conclude our discussion of chromatic quality we present in Fig. 4 simulations of the lighting inside a white office space with TMDC power-generating windows. The simulations have been performed using the open-source software Blender 3D with the Cycles render engine. They show different zones of the office as they would be perceived by a person situated inside of it. Each zone corresponds to a different TMDC absorber thickness and the light sources have been programmed to reproduce in each case the SPD calculated by our optical model (again including direct and indirect sunlight; details are given in the Methods section). The first zone on the left implements a window with no TMDC solar cell. As we move to the right, there are windows with increasing TMDC absorber thickness, and correspondingly lower APT and CRI. The exposition of the image has been increased slightly for the cases with lowest APT emulating an eye pupil or a photography diaphragm that adapts to lower illumination conditions. These simulations confirm that the illumination using TMDC-based photovoltaic windows has a natural and pleasant tone, slightly warmer than the original spectrum. In the case of WSe_2 this is even true for the 30-nm-thick absorber. Although the 55 nm-thick WSe_2 absorber has in principle an acceptable color quality (CRI > 80) the very low CCT produces an unusual effect, as the lighting resembles that of candles. The complete Blender simulated images are shown in the SI, S9.

Table 2
CRI (dimensionless) and APT (percentage) of the transmitted light of different TMDC-based semitransparent power-generating windows on June 21st at 9 AM and December 21st at 11 AM with east-facing and southeast-facing façades in Madrid.

	Thickness (nm)	June 21st,East		Dec. 21st.East		June 21st, Southeast		Dec. 21st. Southeast		Type of illumination
		CRI	APT	CRI	APT	CRI	APT	CRI	APT	
Glass only	-	99	89.2	99	81.2	99	81.2	99	89.3	clear
MoS_2	3	95.6	62.4	94.2	59.0	94.0	59.0	96.0	62.5	clear
	11	92.9	31.2	90.6	31.8	90.2	31.7	93.4	31.1	sun control
	30	–	15.4	–	15.8	–	15.7	–	15.5	colored
WSe_2	3	98.1	68.4	97.9	63.6	98.2	63.7	97.8	68.5	clear
	11	95.7	43.7	95.7	41.7	96.1	41.7	95.2	43.7	sun control
	30	93.7	24.0	93.3	22.8	93.8	22.8	93.2	24.0	sun control
	55	83.9	14.9	82.4	13.1	82.8	13.1	83.6	15.0	sun control

4. Angular acceptance

Having a high angular acceptance is particularly important for photovoltaic semitransparent windows because the incidence of sunlight onto them is generally far from perpendicular. The angle of incidence at a given moment will be determined by the orientation of the façade and the position of the Sun in the sky. To maximize daily production, the layer structure of the TMDC-based semitransparent module has been optimized in all cases assuming an incidence angle of 57°, which approximates the daily average for the latitude of Madrid. Fig. 5 illustrates the variation in absorptance of the solar cell within the photovoltaic window as the incidence angle changes. Different absorber thicknesses are shown for WSe_2 and MoS_2. Remarkably, the absorptance loss is $\leq$ 10 % for any incidence angle between 0° and 75° (70° for the 11-nm-thick MoS_2 absorber). The grey curve shows the reflection from a low-iron glass as the one used at the front of the module structure. Note that this reflection is marginal for angles below 45° and becomes stronger above that value, reaching 25 % at 75°. This curve has been added to illustrate that, as it is the case of any solar cell technology, this reflection is mostly responsible for the decrease in absorptance of the solar cells under sharply slanted incident light. In the case of semitransparent devices, the increase in reflection can affect not only the absorptance but also the APT.

5. Estimated power generation from semitransparent TMDC PV-windows

Fig. 6 shows the transmitted illumination flux, photocurrent, and power density estimated for WSe_2 and MoS_2 semitransparent solar cells with different absorber thicknesses using Madrid sunlight spectra. We calculate the power density absorbed by the TMDC devices inside the semitransparent windows using the same optical model and incident spectrum simulations from previous sections. The device layer structure for a given absorber thickness is also the same as presented above, which has been optimized following the two-criteria algorithm. The visible transmitted illumination flux is obtained from the product of the incident spectrum, the transmittance of the module, and the photopic function. The upper panels in Fig. 6 show that the indoor illumination flux at the plane containing the window surpasses in all cases the 500 lux required by the normative for office spaces [5], even in the moments when only diffuse sunlight is reaching the windows.

The photocurrent and power generation plots show that for thinner absorbers, MoS_2 devices have higher production than WSe_2 devices, and the opposite occurs for thicker absorbers. The generated photocurrent is computed assuming internal quantum efficiency equal to 1 for photons with energy above the direct bandgap energy. The operation temperature is 25 C. The estimated power is obtained from the current density-voltage curve of the device, which is calculated using a generalized Shockley model with a diode equation of ideality factor $n = 1$. The reverse saturation current is estimated using the model of King [51] to set an offset between indirect bandgap energy and open-circuit voltage under AM1.5 G illumination (this model produces a realistic prediction for a high quality photovoltaic device). A generalized Shockley model has been successfully applied before to the simulation of experimental ultrathin devices made of bulk TMDCs, including WSe_2 and MoS_2 junctions [52,53]. Note that the thinnest absorber studied here, 3 nm, falls in the few-layer thickness range for most TMDCs. In this limiting case, the results of the bulk model are only approximate due to the role of excitons in charge transport, and a more accurate power estimation can be obtained using an excitonic model [18].

The model includes variable shunt and series resistances in the solar cell. The data presented in Fig. 6 corresponds to infinite shunt resistance. Since the carrier concentration of the TMDC layers is unknown, the series resistance is modeled assuming that all lateral transport takes place through the ITO layers. We use a sheet resistance for ITO of $1.4{\cdot}10^{-4}$ Ω·cm which is congruent with values for ITO deposited on glass published in the literature [54–56]. We assume that a simple metallic grid is employed for current collection, formed by 50-μm-wide metallic fingers that resemble the low-cost front metal grid found on silicon solar cells. The chosen finger pitch is 0.5 cm, a design that results in a shadow factor of 1 %. From the ITO resistivity and using the expressions given in the SI, section S6, we calculate a device series resistance per unit of ITO thickness of 29 $\Omega{\cdot}cm^2{\cdot}nm$. Therefore, the series resistance is below 1 $\Omega{\cdot}cm^2$ for all the structures studied here (the most and least resistive devices presented in Table 1 having resistances of 0.8 and 0.4 $\Omega{\cdot}cm^2$, respectively). Assuming infinite shunt resistance and 0.5 cm finger pitch, the generalized Shockley model predicts 9.7 % conversion efficiency and 0.78 V open-circuit voltage for a PV window with a 30-nm-thick WSe_2 absorber under AM1.5 G illumination (the theoretical AM1.5 G limits for a cell with that absorber implementing light trapping are 30 % conversion efficiency and 1.3 V open-circuit voltage [28]).

Table 3 displays the results of integrated daily energy output for east- and southeast-facing façades on June 21st and December 21st. The maximum values of energy production are obtained on June 21st for the east-facing configuration. However, the difference in the daily production between December and June is considerably larger in the east orientation than in the southeast orientation. Having a more balanced production throughout the year may be a positive feature. For clear windows (3 nm absorber), MoS_2-based windows perform better, showing around 44 % higher production on June 21st and 27 % on December 21st than WSe_2. By contrast, when it comes to sun control applications, WSe_2-based devices have a larger range of admissible thickness than MoS_2 and thus WSe_2-based devices can provide higher power density output. In any case, the selection of the optimal semitransparent window will in most cases be based on the APT and CRI values required for the building occupation rather than on the energy output.

The output power estimated by our model is influenced by different parameters. Reducing the collection efficiency of the devices (internal quantum efficiency < 1) has a virtually linear effect on power generation. Regarding shunt and series resistance, additional calculations showing their impact are given in the SI, Section S10. Assuming that TMDCs deposited by low-cost techniques have a shunt resistance of 3000 $\Omega{\cdot}cm^2$ - state-of-the-art organic solar cells have values ranging

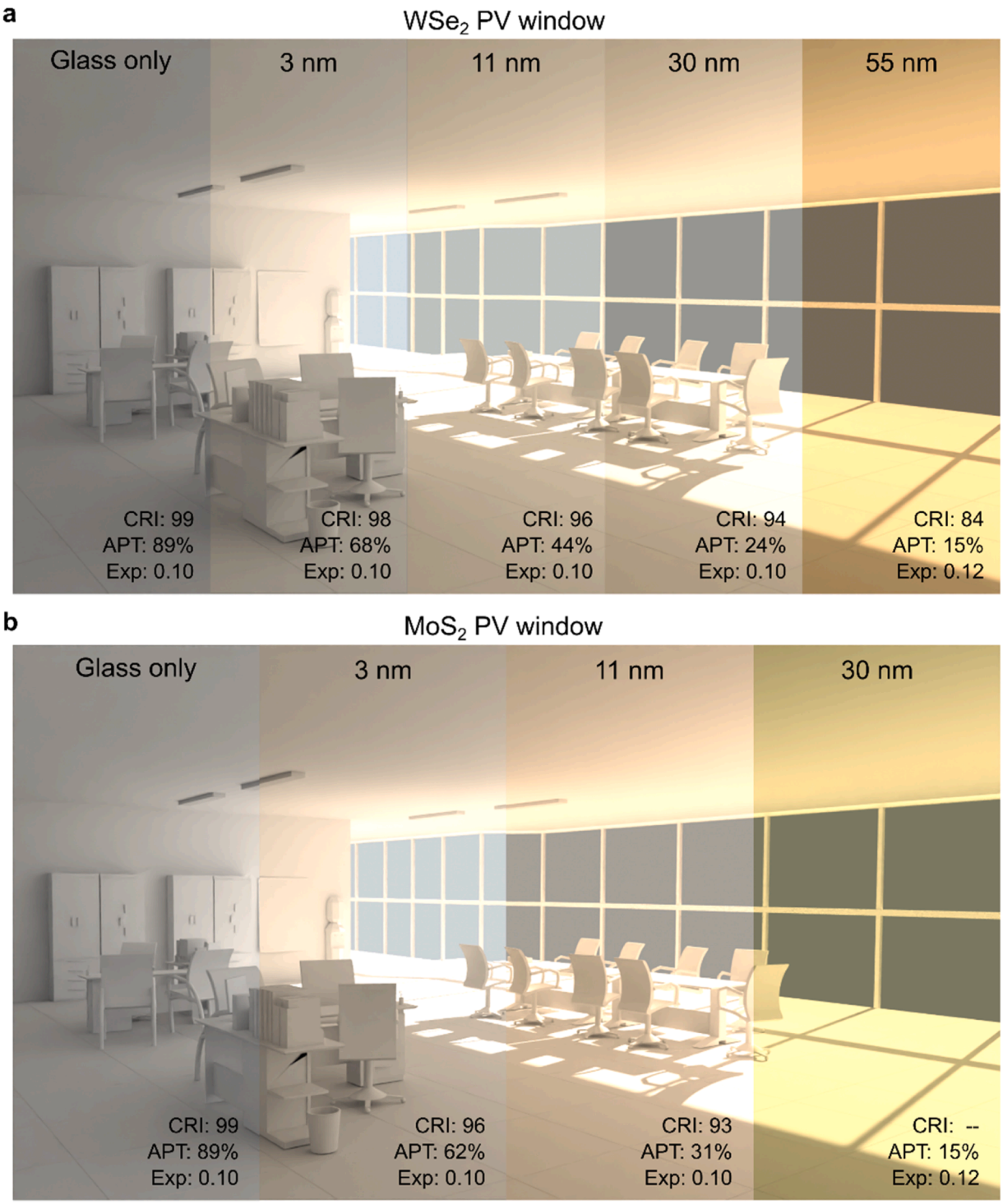

Fig. 4. Blender 3D simulation of the illumination inside an office with different cases of TMDC semitransparent windows for an east-facing façade on June 21st at 9 AM in Madrid. CRI, APT, and exposition level are given for each image. (a) WSe_2 PV windows and (b) MoS_2 PV windows.

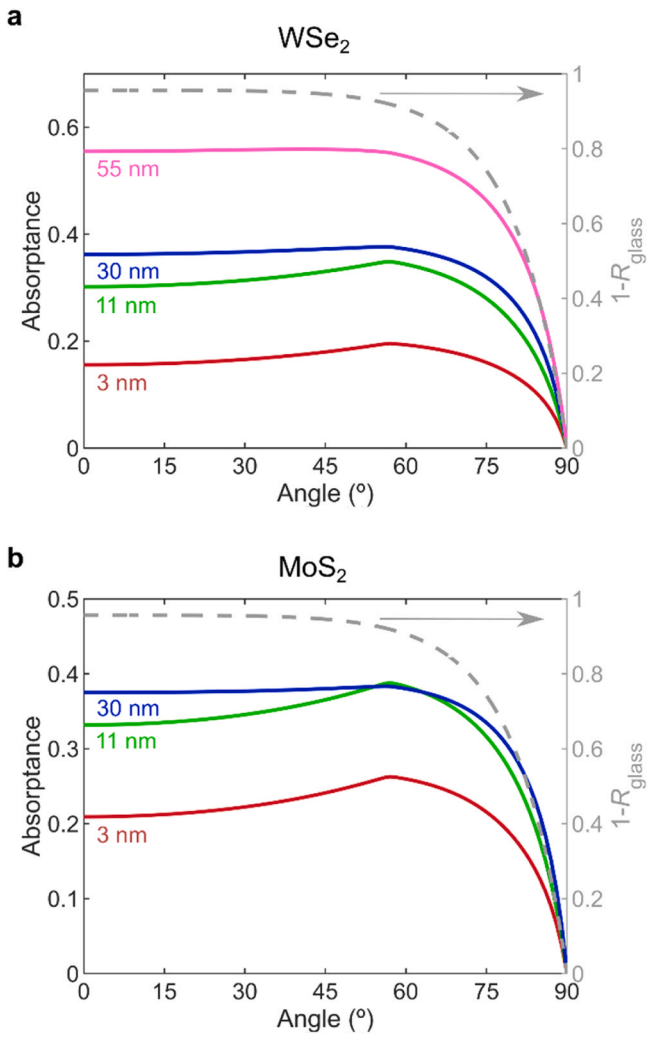

Fig. 5. Absorptance of TMDC absorbers located inside an optimized PV window as a function of the incidence angle. (a) WSe_2. (b) MoS_2. Curve labels indicate the thickness of the absorber. The grey dashed curve represents the fraction of light that is not reflected by the front glass.

from 500 to 3000 Ω·cm^2 [57] - our model predicts energy density losses on the order of 5 %. With respect to series resistance, in the model it is determined by the finger pitch in the metal grid. Increasing it from 0.5 to 1 cm would result in losses of approximately 2 %. However, the loss resulting from a 2 cm pitch is already as high as 10 % for the most resistive devices (those in which the optimal ITO thickness is small). If the aesthetics of the PV window are compromised by the presence of metal fingers, more sophisticated contact technologies can be employed that combine invisibility with low series resistance, such as Ag nanowire meshes or fingers with an engineered shape [58].

Because the incidence angle cannot be optimized for PV windows, geographical latitude significantly affects power generation. Lower latitudes experience more stable energy production throughout the year, while higher latitudes see greater reductions in winter and increases in summer, mostly due to variations in daylight hours. Consequently, lower latitudes produce significantly more energy in winter. For example, an east-facing facade in Madrid (40.5° N) produces 70 Wh/m^2 on December 21st, whereas the same façade in Caracas (10.5° N) generates 165 Wh/m^2, 2.4 times more. Conversely, at a high latitude such as Stockholm (59.3° N), an east-facing facade yields only 11 Wh/m^2 on that day.

In summer, however, production increases at higher latitudes, while it decreases at lower latitudes, as the low zenith angle of the sun is disadvantageous for vertical modules. This effect is noticeable for an east-facing facade (with production in Stockholm, Madrid, and Caracas at 278, 240, and 196 Wh/m^2, respectively) and can be especially dramatic for south-facing facades at low latitudes. Although seasonal effects can partially balance each other, annual production generally increases with decreasing latitude. Additionally, as for any PV technology, climatic factors can greatly influence final energy generation, particularly seasonal cloud coverage. It must be noted that, while the Bird & Riordan solar model includes the effect of aerosols and humidity on the sunlight scattering and absorption, producing realistic solar spectra, our results do not account for the potential impact of cloud cover.

6. Case study: simulation of the power generated by a representative building

We now analyze the application of TMDC-based semitransparent windows in a case study. The building selected is the Picasso Tower, an office building located in Madrid, Spain, with coordinates 40° 24' N, 3° 42' W. Picasso Tower has a height of 157 m and a base dimension of 49.6 ×37.7 m. The larger façades of the building are east-facing and west-facing. We calculate the power consumption of the building basing on the estimation for general offices of 95 kWh/m^2 per year [59]. The office surface in the tower is 71700 m^2 [60], resulting in a daily consumption of 18.66 MWh. We suppose that the east-, south-, and west-facing façades of the building are covered with semitransparent TMDC-based windows for sun control, using the 11-nm-thick MoS_2 absorber or the 30-nm-thick WSe_2 absorber. The APT of these windows is 31–32 % and 23–24 %, respectively (see Table 2). These are low APT values, but they are adequate in sunny locations as Madrid, where direct sunlight needs to be blocked in workspaces. As it is shown in Fig. 6, these windows guarantee the minimum standardized illumination level of 500 lux [5] at the plane of the window in this location even when there is no direct irradiance.

Fig. 7 shows the production of each façade of the Picasso Tower at the different hours of the day on June 21st and December 21st. Since PV windows are placed vertically, south façades are highly productive in the winter but less productive in the summer, when the sun is high in the sky. The opposite applies to east and west façades. Table 4 compiles the predicted daily energy output from the power-generating windows, resulting from the integration of the curves in Fig. 7. For instance, the MoS_2 device when mounted on the east façade produces 205.7 Wh/m^2 on June 21st, which multiplied by a 7787 m^2 area, results in a daily generation of 1.60 MWh. By adding the three facades we obtain a total energy of 3.56 MWh. Similarly, the three facades combined produce 2.36 MWh on December 21st. The WSe_2 absorber exhibits a larger energy output, 4.36 MWh on June 21st and 2.97 MWh on December 21st. These values constitute a fair percentage of the overall energy consumption of the building, between 16 % and 23 %. However, the whole façade can in most cases not be replaced with semitransparent windows. Under a most realistic assumption, we consider a second case, in which two thirds of the façade are covered with semitransparent windows while one third is covered with opaque modules made of the same material (filling, among other areas, the space between floors). In the opaque modules, the TMDC absorber is thicker, and the back ITO layer has been replaced by an aluminum mirror. In the second case, the overall energy production increases by ~ 40 %, leading in the case of WSe_2 on June 21st to an energy share as high as 32 % (data for opaque module estimated production is available in the SI, section S7).

While the energy savings predicted for TMDC-based PV windows are considerable, the energy density generated is lower than that of traditional PV systems due to the semitransparency and the inability to optimize the tilt angle. PV facades, however, can be highly productive on high-rise buildings because of the large surface areas involved. Therefore, for PV glazing development, keeping solar cell fabrication costs particularly low is crucial. In this regard, TMDCs are promising candidates due to potential cost reductions associated with extremely

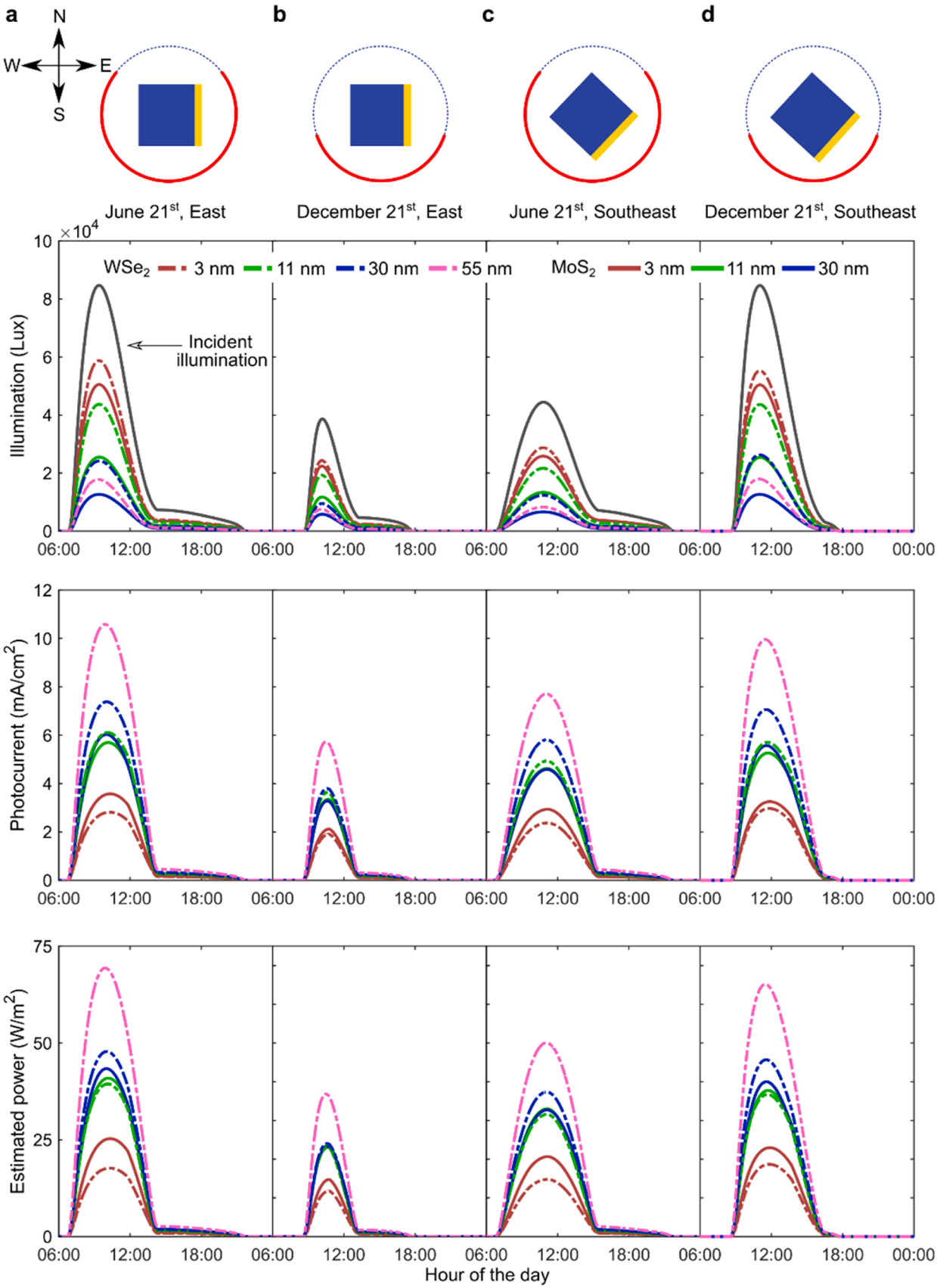

Fig. 6. Indoor illumination intensity, photocurrent and power density throughout the day produced by different optimized PV-windows located in Madrid (absorber thickness is color-coded). (a) East orientation on June 21st. (b) East orientation on December 21st. (c) Southeast orientation on June 21st. (d) Southeast orientation on December 21st. Top: schematics of building orientation with the position of the module (yellow) and solar path (red).

Table 3
Estimated energy density production by different TMDC-based semitransparent power-generating windows on June 21st at 9 AM and December 21st at 11 AM for east-facing and southeast-facing façades in Madrid.

	Thickness (nm)	Estimated daily energy density production (Wh/m^2)				Type of illumination
		21st June, East	21st Dec.,East	21st June, Southeast	21st Dec., Southeast	
MoS_2	3	127	41	111	110	Clear
	11	205	67	179	182	Sun control
	30	215	68	180	189	Colored
WSe_2	3	91	33	81	90	Clear
	11	198	66	171	178	Sun control
	30	240	70	205	220	Sun control
	55	340	108	275	306	Sun control

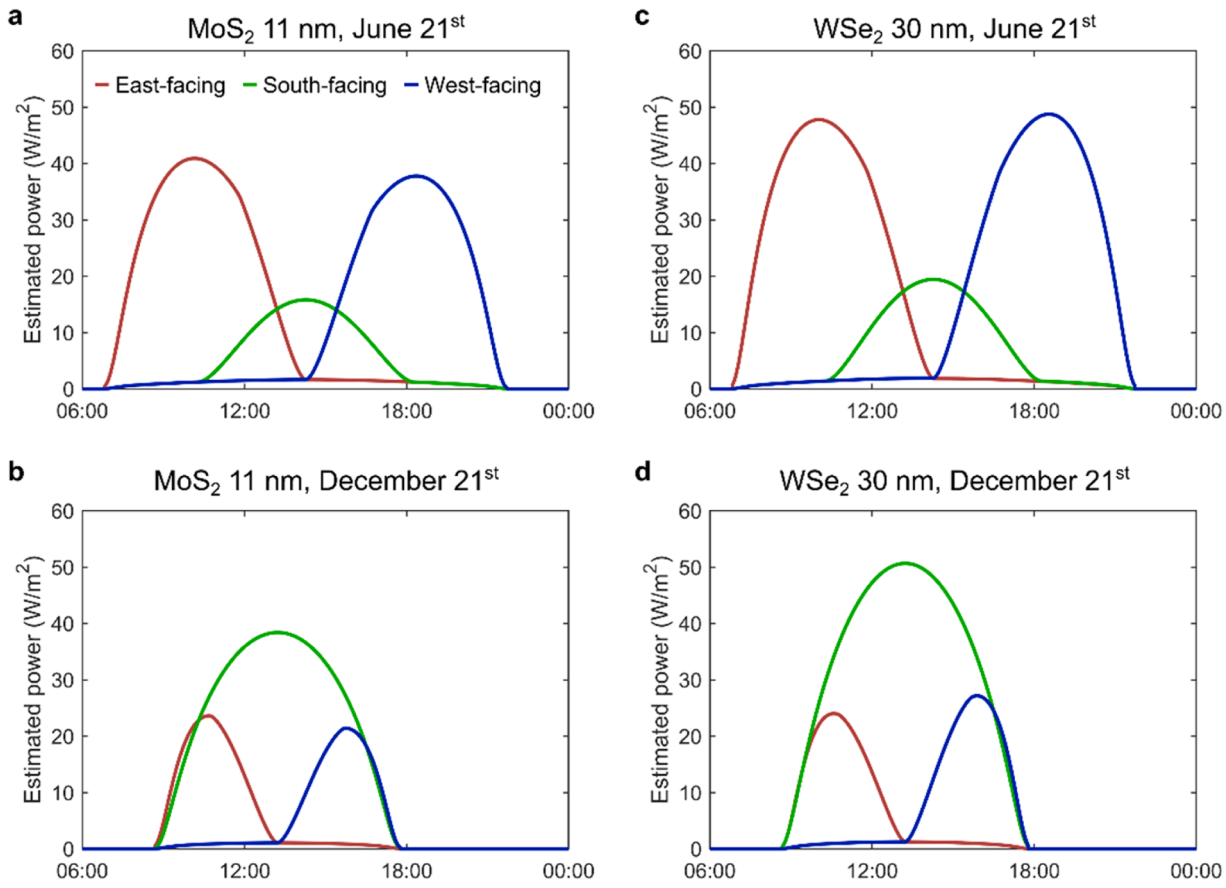

Fig. 7. Estimation of the power density that TMDC–based semitransparent windows would produce on the Picasso Tower. (a) 11-nm-thick MoS_2 absorber on June 21st. (b) 11-nm-thick MoS_2 absorber on December 21st. (c) 30-nm-thick WSe_2 absorber on June 21st. (d) 30-nm-thick WSe_2 absorber on December 21st.

Table 4
Daily energy production and percentage of the building electrical consumption for sun-control PV windows with an 11-nm-thick MoS_2 absorber or a 30-nm-thick WSe_2 absorber. Two cases are shown: only semitransparent modules and semitransparent modules in combination with opaque modules.

	Date	Case 1: façade fully covered with semitransparent PV		Case 2: 2/3 of façade semitransparent PV plus 1/3 opaque modules	
		Energy production (MWh)	% of energy consumption	Energy production (MWh)	% of energy consumption
MoS_2	June 21st	3.56	19.1	4.85	26.0
	December 21st	2.36	12.7	3.31	17.7
WSe_2	June 21st	4.36	23.4	6.15	32.9
	December 21st	2.97	15.9	4.30	23.0

low material use and the availability of low-cost deposition techniques, such as solution processing, which are easily scalable. However, further research is needed to realize this potential in commercial devices.

7. Conclusions

TMDC-based solar cells are excellent candidates for semitransparent applications because their layered crystalline structure enhances the absorption of the long-wavelength range of the visible spectrum. This yields a balanced absorptance of visible light which is not achievable by conventional photovoltaic materials. We have modeled the performance of MoS_2- and WSe_2-based power-generating semitransparent windows, optimizing their layer structure to maximize energy production while assuring the quality of the transmitted light. WSe_2 shows higher energy density production while admitting a wider range of thicknesses without jeopardizing the chromatic characteristics of the transmitted light, and MoS_2 shows better performance when a clear illumination is desired (thin absorbers).

We analyzed the chromaticity of TMDC semitransparent windows using the CIE color space and the ANSI C78.377 standard. The transmitted spectra resemble the emission of a black body whose CCT decreases as the absorber thickness increases. The spectra fulfill the chromatic standards for MoS_2 absorber thickness below 18 nm or WSe_2 absorber thickness below 103 nm. The resulting indoor illumination has high CRI and Blender 3D simulations confirm that it has a pleasant warm tone.

In a case study located in Madrid, Spain, we estimate that using TMDC-based power-generating semitransparent windows could save up to 23 % of the daily energy consumption in a large office building. This percentage rises to 33 % when semitransparent windows are used in combination with opaque modules made of the same TMDC materials. These values of energy production are achieved while keeping optimal illumination conditions inside the building, with a high CRI, an adequate APT, and acceptable luminosity values. TMDC-based semitransparent windows show great potential for building-integrated PV applications and could play an important role in the decarbonization of buildings and the local production of clean energy in urban areas.

Experimental procedures/methods

Optical model: we calculate the light flux as it travels through the multilayer structure, including coherent and incoherent layers, and accounting for multiple reflections and interference [34,42]. Light absorption is calculated from the variation of the Poynting vector at each material interface for coherent layers (TMDC absorber and ITO layers) and the variation of the energy density for incoherent layers (EVA and glass slabs).

The refractive indexes and extinction coefficients have been taken from Refs. [33,35,36,61,62] (see SI, section S1). We include in the model the anisotropy of the TMDC refractive index and extinction coefficient (see SI, section S2) which becomes relevant when the incidence angle is not perpendicular. For the TMDCs, we use bulk optical constants, in contrast to few-layer values. Strictly speaking, this is inaccurate for the thinnest devices discussed here (3 nm thick). For example, MoS_2 layers exhibit bulk optical properties only for thicknesses above 13 monolayers ($\sim$ 8 nm) [63]. However, the scattering in the published values of refractive index for few-layer and monolayer MoS_2 [63–65] surpasses the difference between published values for bulk, few-layers and monolayers. Hence, using the same bulk values for the whole range of thicknesses offers more consistent results.

An inherent condition of PV windows is that they almost always operate under relatively large incidence angles of the solar flux. Our calculations are performed for variable angles, considering the position of the Sun in the sky and the orientation of the façade where the PV window is mounted. In the case of TMDC devices, the angular dependence is complicated by the fact that the refractive indexes of these materials are anisotropic due to their layered crystalline structure [35,36]. We calculate an effective refractive index as a function of the angle of propagation of light inside each layer (details are given in the SI, section S2).

Simulation of incident spectra: we consider the direct and the diffuse spectra. The angle of incidence of the sunlight flux and its spectrum used as input for the optical model are calculated using the equation from Kalogirou [66] (angle of incidence) and from Bird and Riordan [67] (incident spectrum). Direct irradiance is easily modeled using the data extracted from the previous references, but calculating the absorption of diffuse irradiance requires integration over the different angles, considering the anisotropy of the refractive index and extinction coefficient of TMDCs. A more detailed explanation of the model used to calculate the diffuse spectrum and its absorption is available in the SI, section S3.

Blender 3D simulations of indoor illumination: the simulations have been performed using the render engine Cycles. Furniture and building elements were colored as perfect white using a diffuse shader in Cycles. We have used two different light sources: one lamp of parallel rays (sun-type lamp) for the direct lighting and an environmental light for the diffuse lighting. Each light source has been modeled using the RGB components obtained from the tristimulus values XYZ computed from the transmission spectrum of the window. Regarding the power, we fed Cycles with a power value (in W/m^2) obtained by integrating the transmitted spectrum. The environmental lighting power was calibrated using a perfect white diffuse color object illuminated by either a sun-type lamp of power P_1 or an environmental light of strength P_2 of the same RGB color. We find the calibration by obtaining the relation between P_1 and P_2 when the perfect white diffuse color object shows the same color under two different lighting conditions. Finally, the exposure of the film has been modified to mimic the effect of the pupil adjustment. More details on the obtention of the images are available in the SI, section S8.

Power production modeling: the estimation is based on the Shockley diode model and includes shunt and series resistance simulation as described in the SI, section S6.

Resource availability:

Lead contact: Elisa Antolín.

Materials availability: No materials have been generated in this study.

Data and code availability: the code for optical model is available in the GitHub repository, see Ref. [44]. Data is available from the lead contact upon request.

CRediT authorship contribution statement

Carlos Bueno-Blanco: Writing – original draft, Visualization, Investigation. **Francisco M. Gomez-Campos:** Writing – review & editing, Visualization, Formal analysis. **Simon A. Svatek:** Writing – review & editing, Visualization, Supervision, Software, Methodology. **Elisa Antolin:** Writing – original draft, Supervision, Project administration, Methodology, Funding acquisition, Conceptualization. **Antonio Marti:** Writing – review & editing, Project administration, Funding acquisition.

Declaration of Competing Interest

The authors declare that they have no known competing financial interests or personal relationships that could have appeared to influence the work reported in this paper

Acknowledgments

The authors acknowledge the support from the MAD2D-CM-UPM Project funded by Comunidad de Madrid, by the Recovery, Transformation and Resilience Plan, and by NextGenerationEU from the European Union. The authors also acknowledge the support from grant

PID2021-124193OB-C21 (PVBooster) funded by MCIN/AEI/10.13039/501100011033 and "ERDF A way of making Europe". F. M. G. C. gratefully acknowledges grant C-ING-208-UGR23 funded by Consejería de Universidad, Investigación e Innovación and by ERDF Andalusia Program 2021-2027.

Appendix A. Supporting information

Supplementary data associated with this article can be found in the online version at doi:10.1016/j.nanoen.2024.110483.

References

[1] Informe Anual de Consumos Energéticos, Instituto para la Diversificación y Ahorro de la Energía (IDAE), Ministerio para la Transición Ecológica y el Reto Demográfico, Gobierno De España. 2019.
[2] T.E. Kuhn, C. Erban, M. Heinrich, J. Eisenlohr, F. Ensslen, D.H. Neuhaus, Review of technological design options for building integrated photovoltaics (BIPV), Energy Build. 231 (2021) 110381, https://doi.org/10.1016/j.enbuild.2020.110381.
[3] B. Norton, P.C. Eames, T.K. Mallick, M.J. Huang, S.J. McCormack, J.D. Mondol, Y. G. Yohanis, Enhancing the performance of building integrated photovoltaics, Sol. Energy 85 (2011) 1629–1664, https://doi.org/10.1016/j.solener.2009.10.004.
[4] P. Bonomo, A. Chatzipanagi, F. Frontini, Overview and analysis of current BIPV products: new criteria for supporting the technological transfer in the building sector, VITRUVIO - Int. J. Archit. Technol. Sustain. (2015) 67–85, https://doi.org/10.4995/vitruvio-ijats.2015.4476.
[5] Light and lighting. Lighting of work places and indoor work places. EN 12464-1: 2021", Technical Comittee CEN/TC 169 "Light and lighting", 2021.
[6] R. Danks, J. Good, R. Sinclair, Assessing reflected sunlight from building facades: a literature review and proposed criteria, Build. Environ. 103 (2016) 193–202, https://doi.org/10.1016/j.buildenv.2016.04.017.
[7] C. Hong, Y. Wang, Z. Gu, C.W. Yu, Cool facades to mitigate urban heat island effects, Indoor Built Environ. 31 (2022) 2373–2377, https://doi.org/10.1177/1420326X221115369.
[8] B. Petter Jelle, C. Breivik, H. Drolsum Røkenes, Building integrated photovoltaic products: a state-of-the-art review and future research opportunities, Sol. Energy Mater. Sol. Cells 100 (2012) 69–96, https://doi.org/10.1016/j.solmat.2011.12.016.
[9] K. Lee, N. Kim, K. Kim, H.-D. Um, W. Jin, D. Choi, J. Park, K.J. Park, S. Lee, K. Seo, Neutral-colored transparent crystalline silicon photovoltaics, Joule 4 (2020) 235–246, https://doi.org/10.1016/j.joule.2019.11.008.
[10] R. Yang, C.-H. Lee, B. Cui, A. Sazonov, Flexible semi-transparent a-Si:H pin solar cells for functional energy-harvesting applications, Mater. Sci. Eng.: B 229 (2018) 1–5, https://doi.org/10.1016/j.mseb.2017.12.005.
[11] E. Pascual-San José, A. Sánchez-Díaz, M. Stella, E. Martínez-Ferrero, M.I. Alonso, M. Campoy-Quiles, Comparing the potential of different strategies for colour tuning in thin film photovoltaic technologies, Sci. Technol. Adv. Mater. 19 (2018) 823–835, https://doi.org/10.1080/14686996.2018.1530050.
[12] G.E. Eperon, V.M. Burlakov, A. Goriely, H.J. Snaith, Neutral color semitransparent microstructured perovskite solar cells, ACS Nano 8 (2014) 591–598, https://doi.org/10.1021/nn4052309.
[13] Y. Li, X. Guo, Z. Peng, B. Qu, H. Yan, H. Ade, M. Zhang, S.R. Forrest, Color-neutral, semitransparent organic photovoltaics for power window applications, Proc. Natl. Acad. Sci. 117 (2020) 21147–21154, https://doi.org/10.1073/pnas.2007799117.
[14] L. Britnell, R.M. Ribeiro, A. Eckmann, R. Jalil, B.D. Belle, A. Mishchenko, Y.-J. Kim, R.V. Gorbachev, T. Georgiou, S.V. Morozov, A.N. Grigorenko, A.K. Geim, C. Casiraghi, A.H.C. Neto, K.S. Novoselov, Strong light-matter interactions in heterostructures of atomically thin films, Science 340 (2013) 1311–1314, https://doi.org/10.1126/science.1235547.
[15] K. Mak, C. Lee, J. Hone, J. Shan, T. Heinz, Phys. Rev. Lett. 105 (2010) 136805, https://doi.org/10.1103/PhysRevLett.105.136805.
[16] A.K. Geim, I.V. Grigorieva, Van der Waals heterostructures, Nature 499 (2013) 419–425, https://doi.org/10.1038/nature12385.
[17] W.M. Haynes, D.R. Lide, T.J. Bruno, Abundance of elements in the earth's crust and in the sea, CRC Handbook of Chemistry and Physics, Taylor & Francis group, CRC Press, Boca Raton, FL, 2016.
[18] Z. Hu, D. Lin, J. Lynch, K. Xu, D. Jariwala, How good can 2D excitonic solar cells be? Device 1 (2023) https://doi.org/10.1016/j.device.2023.100003.
[19] K.S. Novoselov, A. Mishchenko, A. Carvalho, A.H. Castro Neto, 2D materials and van der Waals heterostructures, Science 353 (2016) aac9439, https://doi.org/10.1126/science.aac9439.
[20] C.-H. Lee, G.-H. Lee, A.M. van der Zande, W. Chen, Y. Li, M. Han, X. Cui, G. Arefe, C. Nuckolls, T.F. Heinz, J. Guo, J. Hone, P. Kim, Atomically thin p–n junctions with van der Waals heterointerfaces, Nat. Nanotech. 9 (2014) 676–681, https://doi.org/10.1038/nnano.2014.150.
[21] M.M. Furchi, A. Pospischil, F. Libisch, J. Burgdörfer, T. Mueller, Photovoltaic effect in an electrically tunable van der Waals heterojunction, Nano Lett. 14 (2014) 4785–4791, https://doi.org/10.1021/nl501962c.
[22] R. Frisenda, A.J. Molina-Mendoza, T. Mueller, A. Castellanos-Gomez, H.S.J. van der Zant, Atomically thin p–n junctions based on two-dimensional materials, Chem. Soc. Rev. 47 (2018) 3339–3358, https://doi.org/10.1039/C7CS00880E.
[23] J. Wong, D. Jariwala, G. Tagliabue, K. Tat, A.R. Davoyan, M.C. Sherrott, H. A. Atwater, High photovoltaic quantum efficiency in ultrathin van der waals heterostructures, ACS Nano 11 (2017) 7230–7240, https://doi.org/10.1021/acsnano.7b03148.
[24] S.A. Svatek, C. Bueno-Blanco, D.-Y. Lin, J. Kerfoot, C. Macías, M.H. Zehender, I. Tobías, P. García-Linares, T. Taniguchi, K. Watanabe, P. Beton, E. Antolín, High open-circuit voltage in transition metal dichalcogenide solar cells, Nano Energy 79 (2021) 105427, https://doi.org/10.1016/j.nanoen.2020.105427.
[25] K. Nassiri Nazif, A. Daus, J. Hong, N. Lee, S. Vaziri, A. Kumar, F. Nitta, M.E. Chen, S. Kananian, R. Islam, K.-H. Kim, J.-H. Park, A.S.Y. Poon, M.L. Brongersma, E. Pop, K.C. Saraswat, High-specific-power flexible transition metal dichalcogenide solar cells, Nat. Commun. 12 (2021) 7034, https://doi.org/10.1038/s41467-021-27195-7.
[26] Z. Zhou, J. Lv, C. Tan, L. Yang, Z. Wang, Emerging frontiers of 2D transition metal dichalcogenides in photovoltaics solar cell, Adv. Funct. Mater. 34 (2024) 2316175, https://doi.org/10.1002/adfm.202316175.
[27] S. Aftab, M.Z. Iqbal, S. Hussain, H.H. Hegazy, M.A. Saeed, Transition metal dichalcogenides solar cells and integration with perovskites, Nano Energy 108 (2023) 108249, https://doi.org/10.1016/j.nanoen.2023.108249.
[28] K. Nassiri Nazif, F.U. Nitta, A. Daus, K.C. Saraswat, E. Pop, Efficiency limit of transition metal dichalcogenide solar cells, Commun. Phys. 6 (2023) 1–11, https://doi.org/10.1038/s42005-023-01447-y.
[29] K.M. Neilson, S. Hamtaei, K. Nassiri Nazif, J.M. Carr, S. Rahimisheikh, F.U. Nitta, G. Brammertz, J.L. Blackburn, J. Hadermann, K.C. Saraswat, O.G. Reid, B. Vermang, A. Daus, E. Pop, Toward mass production of transition metal dichalcogenide solar cells: scalable growth of photovoltaic-grade multilayer WSe_2 by Tungsten selenization, ACS Nano 18 (2024) 24819–24828, https://doi.org/10.1021/acsnano.4c03590.
[30] Blender 3D (version 3.1.0) [Computer software], Blender Delopment Team, 2022.
[31] H. Yang, A. Giri, S. Moon, S. Shin, J.-M. Myoung, U. Jeong, Highly scalable synthesis of MoS_2 thin films with precise thickness control via polymer-assisted deposition, Chem. Mater. 29 (2017) 5772–5776, https://doi.org/10.1021/acs.chemmater.7b01605.
[32] J. Suh, T.-E. Park, D.-Y. Lin, D. Fu, J. Park, H.J. Jung, Y. Chen, C. Ko, C. Jang, Y. Sun, R. Sinclair, J. Chang, S. Tongay, J. Wu, Doping against the native propensity of MoS_2: degenerate hole doping by cation substitution, Nano Lett. 14 (2014) 6976–6982, https://doi.org/10.1021/nl503251h.
[33] M. Rubin, Optical properties of soda lime silica glasses, Sol. Energy Mater. 12 (1985) 275–288, https://doi.org/10.1016/0165-1633(85)90052-8.
[34] C. Bueno-Blanco, S.A. Svatek, E. Antolin, High broadband light absorption in ultrathin MoS_2 homojunction solar cells, Opt. Express, OE 30 (2022) 42678–42695, https://doi.org/10.1364/OE.469931.
[35] G.A. Ermolaev, D.V. Grudinin, Y.V. Stebunov, K.V. Voronin, V.G. Kravets, J. Duan, A.B. Mazitov, G.I. Tselikov, A. Bylinkin, D.I. Yakubovsky, S.M. Novikov, D. G. Baranov, A.Y. Nikitin, I.A. Kruglov, T. Shegai, P. Alonso-González, A. N. Grigorenko, A.V. Arsenin, K.S. Novoselov, V.S. Volkov, Giant optical anisotropy in transition metal dichalcogenides for next-generation photonics, Nat. Commun. 12 (2021) 854, https://doi.org/10.1038/s41467-021-21139-x.
[36] B. Munkhbat, P. Wróbel, T.J. Antosiewicz, T.O. Shegai, Optical constants of several multilayer transition metal dichalcogenides measured by spectroscopic ellipsometry in the 300–1700 nm range: high index, anisotropy, and hyperbolicity, ACS Photonics 9 (2022) 2398–2407, https://doi.org/10.1021/acsphotonics.2c00433.
[37] M. Gloeckler, J.R. Sites, Band-gap grading in $Cu(In,Ga)Se_2$ solar cells, J. Phys. Chem. Solids 66 (2005) 1891–1894, https://doi.org/10.1016/j.jpcs.2005.09.087.
[38] R.E. Treharne, A. Seymour-Pierce, K. Durose, K. Hutchings, S. Roncallo, D. Lane, Optical design and fabrication of fully sputtered CdTe/CdS solar cells, J. Phys.: Conf. Ser. 286 (2011) 012038, https://doi.org/10.1088/1742-6596/286/1/012038.
[39] L.J. Phillips, A.M. Rashed, R.E. Treharne, J. Kay, P. Yates, I.Z. Mitrovic, A. Weerakkody, S. Hall, K. Durose, Dispersion relation data for methylammonium lead triiodide perovskite deposited on a (100) silicon wafer using a two-step vapour-phase reaction process, Data Brief. 5 (2015) 926–928, https://doi.org/10.1016/j.dib.2015.10.026.
[40] D.E. Aspnes, A.A. Studna, Dielectric functions and optical parameters of Si, Ge, GaP, GaAs, GaSb, InP, InAs, and InSb from 1.5 to 6.0 eV, Phys. Rev. B 27 (1983) 985–1009, https://doi.org/10.1103/PhysRevB.27.985.
[41] S. Wang, B.D. Weil, Y. Li, K.X. Wang, E. Garnett, S. Fan, Y. Cui, Large-area free-standing ultrathin single-crystal silicon as processable materials, Nano Lett. 13 (2013) 4393–4398, https://doi.org/10.1021/nl402230v.
[42] E. Centurioni, Generalized matrix method for calculation of internal light energy flux in mixed coherent and incoherent multilayers, Appl. Opt., AO 44 (2005) 7532–7539, https://doi.org/10.1364/AO.44.007532.
[43] M.A. Kats, R. Blanchard, P. Genevet, F. Capasso, Nanometre optical coatings based on strong interference effects in highly absorbing media, Nat. Mater. 12 (2013) 20–24, https://doi.org/10.1038/nmat3443.
[44] S. Svatek, C. Bueno-Blanco, E. Antolin, GitHub repository, ⟨https://github.com/simonsvatek/Photovoltaic-windows-based-on-transition-metal-sichacogenides-producing-natural-light-spectra/⟩, 2024.
[45] CIE Standard Illuminants for Colorimetry. ISO 10526:1999/CIE S005/E-1998", International Comission on Illumination, 1999.
[46] J.M. Llorens, J. Buencuerpo, P.A. Postigo, Absorption features of the zero frequency mode in an ultra-thin slab, Appl. Phys. Lett. 105 (2014) 231115, https://doi.org/10.1063/1.4904027.

[47] ANSI C78.377-2017 - Electric Lamps - Specifications for the Chromaticity of Solid-State Lighting Products", ⟨https://webstore.ansi.org/standards/nema/ansic783772017⟩.
[48] M. Debije, Better luminescent solar panels in prospect, Nature 519 (2015) 298–299, https://doi.org/10.1038/519298a.
[49] V.V. Plotnikov, C.W. Carter, J.M. Stayancho, N.R. Paudel, H. Mahabaduge, D. Kwon, C.R. Grice, A.D. Compaan, Semitransparent PV windows with sputtered CdS/CdTe thin films, IEEE 39th Photovolt. Spec. Conf. (PVSC) 2013 (2013) 0405–0408, https://doi.org/10.1109/PVSC.2013.6744178.
[50] C.J. Traverse, R. Pandey, M.C. Barr, R.R. Lunt, Emergence of highly transparent photovoltaics for distributed applications, Nat. Energy 2 (2017) 849–860, https://doi.org/10.1038/s41560-017-0016-9.
[51] R.R. King, D. Bhusari, A. Boca, D. Larrabee, X.-Q. Liu, W. Hong, C.M. Fetzer, D. C. Law, N.H. Karam, Band gap-voltage offset and energy production in next-generation multijunction solar cells, Prog. Photovolt.: Res. Appl. 19 (2011) 797–812, https://doi.org/10.1002/pip.1044.
[52] D.J. Groenendijk, M. Buscema, G.A. Steele, S. Michaelis de Vasconcellos, R. Bratschitsch, H.S.J. van der Zant, A. Castellanos-Gomez, Photovoltaic and Photothermoelectric Effect in a Double-Gated WSe_2 Device, Nano Lett. 14 (2014) 5846–5852, https://doi.org/10.1021/nl502741k.
[53] S.A. Svatek, E. Antolin, D.-Y. Lin, R. Frisenda, C. Reuter, A.J. Molina-Mendoza, M. Muñoz, N. Agraït, T.-S. Ko, D.P. de Lara, A. Castellanos-Gomez, Gate tunable photovoltaic effect in MoS_2 vertical p–n homostructures, J. Mater. Chem. C. 5 (2017) 854–861, https://doi.org/10.1039/C6TC04699A.
[54] S. Ishibashi, Y. Higuchi, Y. Ota, K. Nakamura, Low resistivity indium–tin oxide transparent conductive films. II. Effect of sputtering voltage on electrical property of films, J. Vac. Sci. Technol. A 8 (1990) 1403–1406, https://doi.org/10.1116/1.576890.
[55] J.P. Zheng, H.S. Kwok, Low resistivity indium tin oxide films by pulsed laser deposition, Appl. Phys. Lett. 63 (1993) 1–3, https://doi.org/10.1063/1.109736.
[56] R.N. Joshi, V.P. Singh, J.C. McClure, Characteristics of indium tin oxide films deposited by r.f. magnetron sputtering, Thin Solid Films 257 (1995) 32–35, https://doi.org/10.1016/0040-6090(94)06331-1.
[57] D. Qin, M. Qiu, X. Zhan, Determining shunt resistances via modeling the photovoltaic performance of organic solar cells, J. Mater. Chem. A 12 (2024) 15063–15070, https://doi.org/10.1039/D3TA08029C.
[58] P. Kumar, S. You, A. Vomiero, Recent progress in materials and device design for semitransparent photovoltaic technologies, Adv. Energy Mater. 13 (2023) 2301555, https://doi.org/10.1002/aenm.202301555.
[59] Energy Benchmarks. CIBSE TM46: 2008., The Chartered Institution of Building Services Engineers, London, UK, ⟨https://www.cibse.org/knowledge-research/knowledge-portal/tm46-energy-benchmarks⟩, 2008.
[60] "Torre Picasso - Ficha, Fotos y Planos", ⟨https://web.archive.org/web/20240308145246/https://es.wikiarquitectura.com/edificio/torre-picasso/⟩.
[61] T.A.F. König, P.A. Ledin, J. Kerszulis, MahmoudA. Mahmoud, M.A. El-Sayed, J. R. Reynolds, V.V. Tsukruk, Electrically tunable plasmonic behavior of nanocube–polymer nanomaterials induced by a redox-active electrochromic polymer, ACS Nano 8 (2014) 6182–6192, https://doi.org/10.1021/nn501601e.
[62] M.R. Vogt, H. Holst, H. Schulte-Huxel, S. Blankemeyer, R. Witteck, D. Hinken, M. Winter, B. Min, C. Schinke, I. Ahrens, M. Köntges, K. Bothe, R. Brendel, Optical constants of UV transparent EVA and the impact on the PV module output power under realistic irradiation, Energy Procedia 92 (2016) 523–530, https://doi.org/10.1016/j.egypro.2016.07.136.
[63] B. Song, H. Gu, M. Fang, X. Chen, H. Jiang, R. Wang, T. Zhai, Y.-T. Ho, S. Liu, Layer-dependent dielectric function of wafer-scale 2D MoS_2, Adv. Opt. Mater. 7 (2019) 1801250, https://doi.org/10.1002/adom.201801250.
[64] G.A. Ermolaev, Y.V. Stebunov, A.A. Vyshnevyy, D.E. Tatarkin, D.I. Yakubovsky, S. M. Novikov, D.G. Baranov, T. Shegai, A.Y. Nikitin, A.V. Arsenin, V.S. Volkov, Broadband optical properties of monolayer and bulk MoS_2, Npj 2D Mater. Appl. 4 (2020) 1–6, https://doi.org/10.1038/s41699-020-0155-x.
[65] C. Hsu, R. Frisenda, R. Schmidt, A. Arora, S.M. de Vasconcellos, R. Bratschitsch, H. S.J. van der Zant, A. Castellanos-Gomez, Thickness-Dependent Refractive Index of 1L, 2L, and 3L MoS_2, $MoSe_2$, WS_2, and WSe_2, Adv. Opt. Mater. 7 (2019) 1900239, https://doi.org/10.1002/adom.201900239.
[66] S.A. Kalogirou, Chapter 2 - Environmental Characteristics, in: S.A. Kalogirou (Ed.), Solar Energy Engineering (Second Edition), Academic Press, Boston, 2014: pp. 51–123. https://doi.org/10.1016/B978-0-12-397270-5.00002-9.
[67] R.E. Bird, C. Riordan, Simple solar spectral model for direct and diffuse irradiance on horizontal and tilted planes at the earth's surface for cloudless atmospheres, J. Clim. Appl. Meteorol. 25 (1986) 87–97. ⟨http://www.jstor.org/stable/26182461⟩.